A Modern VLF Radio Receiver Designed for the Array for VLF Imaging of the D-Region (AVID)

James M. Cannon, *Graduate Student Member, IEEE*, Ryan Dick, Bennett Fragomeni, Hayden Gebhardt, Sebastian Wankmueller, Ash Tribble, Sophia Orlandella, Max Feinland, and Robert A. Marshall, *Senior Member, IEEE*

***Abstract*—Very-low-frequency (VLF) radio waves are commonly used to remotely sense the D-region ionosphere. In the past few decades, a few prominent designs for VLF receivers have come to the forefront of the community, such as the AWESOME receiver developed at Stanford in the early 2000s. In the last decade, advancements in off-the-shelf electrical components and the obsoletion of others motivated a redesign of this receiver system. The result of this receiver design work is presented in this article with the measured characteristics of over ten complete systems. The newly operational array for VLF imaging of the D-region (AVID), incorporating the updated VLF receiver, is also presented. One early result from AVID is the characterization of the drift rates of the phase of two VLF transmitters. The NLK transmitter at 24.8 kHz was found to drift by −0.07886°/s ± 0.00083°/s, while the NML transmitter at 25.2 kHz was found to drift by −0.07201°/s ± 0.00019°/s. We also show that the transmitted power of these transmitters can change over time, by up to ∼7% in the case of NLK. Finally, two early case studies are presented, showing AVID's ability to observe and track: 1) the effects of an M7.2 solar flare on the D-region ionosphere and 2) the onset of a −333 nT Dst geomagnetic storm and the D-region's response to it. These case studies demonstrate the tools necessary for future work incorporating spatial estimation algorithms to better characterize disturbances to the D-region ionosphere.**

***Index Terms*—D-region ionosphere, instrumentation, subionospheric remote sensing, very low frequency (VLF).**

I. Introduction

SPACE weather encompasses dynamic phenomena from the solar corona to the Earth's upper atmosphere and the responses of these regions to solar activity. Measuring these coupled processes throughout the heliosphere provides insights into the complex underlying mechanisms contributing to the evolution of phenomena such as solar flares, coronal mass ejections, disturbances to the solar wind, and their eventual coupling to Earth's systems. Earth's ionosphere forms the transition region between the space environment and Earth's upper atmosphere, sensitive both to neutral winds below and solar impacts above. Its name comes from the mobile ions and electrons within this environment; the ionosphere is composed of a plasma of varying density. The ionosphere is classically divided into three regions: the D- (60–90 km), E- (90–150 km), and F-regions (150–500 km) [1].

Coupled both to the magnetosphere through particle precipitation and transport [2], [3] and to the mesosphere and stratosphere below through transport, atmospheric chemistry, and waves propagating from below [4], [5], the D-region is of key interest to geoscientists. One important interaction is stratospheric ozone depletion caused by interactions with odd nitrogen (NO_x) and odd hydrogen (HO_x), both of which are produced by energetic particle precipitation (EPP) from the magnetosphere into the upper atmosphere [4], [5]. While known to be a prevalent phenomenon, modeling efforts do not sufficiently capture the effects of EPP on the production of NO_x and HO_x in the mesosphere [6]. In part, this comes from the lack of good measurements of higher energy EPP [7]. The lowest region of the ionosphere, the D-region, is only sensitive to the precipitation of electrons with energies above ∼30 keV [1], [8]. As such, continuous measurements of the D-region are highly desirable to improve atmospheric models that incorporate EPP.

The combination of low plasma density and altitude range from 60 to 90 km makes the D-region of the ionosphere particularly challenging to measure. The D-region is too high for direct balloon measurements while simultaneously too low for in situ satellite measurements. Sounding rocket campaigns have provided brief in situ observations of the D-region, that when aggregated, as in the work leading to the Faraday International Reference Ionosphere (FIRI), can provide a statistical picture of the D-region but are inadequate for long-duration studies or analysis of significant precipitation events [9], [10]. Turning to remote observation techniques, the D-region density is too sparse for incoherent scatter radar (ISR) measurements, except during significant enhancements [11]. Riometer-based electron density inversions use HF absorption through the D-region but are spatially limited to a cone directly above the instruments [12] and are not conducive to estimating an electron density profile versus altitude.

Instead, the D-region is commonly studied by remotely sensing with radio waves (see [13]). In particular, very-low-frequency (VLF, 3–30 kHz) radio remote sensing is uniquely suited to continuous measurement of the D-region dynamics. Bounded above by the D-region plasma and below by the

Received 22 May 2025; revised 29 July 2025; accepted 1 September 2025. Date of publication 8 September 2025; date of current version 18 September 2025. This work was supported by the National Science Foundation through the Faculty Early Career Development (CAREER) Program under Grant 2044846. *(Corresponding author: James M. Cannon.)*

The authors are with the Ann and H.J. Smead Department of Aerospace Engineering Sciences, University of Colorado Boulder, Boulder, CO 80303 USA (e-mail: James.Cannon-1@colorado.edu).

Digital Object Identifier 10.1109/TGRS.2025.3607146

conducting Earth, VLF waves reflect within the Earth–ionosphere (EI) waveguide and can propagate with minimal losses on a global scale (attenuation of ~2 dB/Mm) [13]. For any given path from a VLF wave transmitter to a measuring receiver, the ground conductivity is constant, which allows any changes in the measured radio wave to be directly tied to changes in ionospheric properties [14], [15]. These measurements can provide continuous monitoring of the D-region ionosphere, in contrast to the statistical picture provided by FIRI, and over a broader region than Riometer inversions can cover. However, a single transmitter–receiver pair lacks geospatial sensitivity along the path, that is, the observed changes to the received signal can be caused by ionospheric changes anywhere along the path. Combining multiple receivers measuring two or more VLF sources (transmitters or sferics), when done carefully, allows for geospatial variance to be observed in the D-region [16], [17], [18], [19], [20], [21], [22], [23], [24], [25], [26], [27].

In this article, we address the D-region spatial estimation problem using an array of VLF receivers deployed over a large region of western Canada. The array of receivers forms a tomographic array, from which the properties of the ionosphere can be estimated within the enclosed geographic region. This article describes the new VLF receiver that was developed specifically for this array, gives an overview of the array design, and presents two preliminary case studies that illustrate the array's capability.

II. Background

Two primary terrestrial sources of VLF signals have been used to study the ionosphere. First, a global network of single-frequency VLF transmitters, used primarily for naval communication, provides narrowband signals that can be continuously monitored. This anthropogenic source of VLF radiation has been used to study lightning-induced electron precipitation (LEP) [13], [28], [29], auroral particle precipitation [30], the transition from day to night as the terminator crosses a path [31], [32], solar flares [33], [34], [35], solar eclipses [36], [37], [38], and more. In addition to space weather studies, VLF measurements have been used to investigate acoustic gravity waves as well as long-period planetary waves [15], [39], [40]. Additionally, perturbations to VLF signals have been linked to possible precursor activity to earthquakes [41], [42], [43], although this is somewhat contested [44], [45]. These narrowband sources are ideal for continuous monitoring of the lower ionosphere and for probing the reflection height at the specific transmitter frequencies. By contrast, broadband lightning-generated radio atmospherics, or "sferics," can be used to probe a range of reflection heights across a broad frequency range simultaneously [46], [47], [48]. These sferics are the dominant source of broadband radiation in the ELF/VLF/LF frequency range. Not only can they be used to measure the lower ionosphere, but these radio emissions also drive changes to ionospheric density through direct heating and ionization and through LEP [13], [49], [50]. LEP is caused when lightning-generated whistler mode waves propagate, either ducted or nonducted by plasma irregularities, through the magnetosphere and scatter energetic electrons, causing them to be lost into the upper atmosphere [13], [51]. In addition to using lightning-generated sferics to probe the ionosphere, VLF receivers have been used to geolocate lightning from broadband measurements [52], [53], [54], [55] as well as to investigate possible radio emissions from meteors [56].

Radio receivers in the VLF range (3–30 kHz) have been used for over 60 years to study ionospheric dynamics (see [57]). A variety of instruments exist for measuring VLF waves; in this work, we focus on orthogonal air-core loop antennas, which measure the transverse magnetic field of propagating VLF waves. While a variety of VLF receivers are used to study the ionosphere (e.g., AbsPAL [58], the Wuhan VLF receiver [59], and the compact multichannel long-wave wideband direction-finding system (CLWDS) [60]), this work details improvements to the Atmospheric Weather Electromagnetic System for Observation, Modeling, and Education (AWESOME) VLF receiver [61], [62] developed at Stanford in the 2000s. Interested readers are directed to [63], which overviews the historical development of VLF receivers as well as additional receiver topologies not discussed in this article. Our updated receiver system has been redesigned with considerations for cost, power, complexity, and reliability. Additionally, robust calibration procedures are discussed. Software integration tools allow for remote operation, automatic data retrieval, and support open science initiatives through data availability.

III. VLF Receiver System

The VLF receiver presented here was designed for use in the array for VLF imaging of the D-region (AVID, discussed in Section V) and is referred to as the AVID receiver. The AVID receiver, like the AWESOME receiver, contains three primary elements: a pair of orthogonal air-core loop antennas, a preamplifier, and a line receiver. These components, shown in Fig. 1, acquire VLF signals, amplify and filter them, and finally process them into digitized data.

The two air-core loop antennas are orthogonally oriented to each other and to the ground plane to measure magnetic field variations in both horizontal axes. As the transverse electric field of a wave propagating within the EI waveguide is close to zero at ground level, this setup of magnetic antennas is sufficient to capture the full amplitude of VLF signals propagating through the EI waveguide. While the instruments in use today make use solely of these two channels of input data, the hardware is designed to support a third channel as needed, which could be either a vertical electric field sensor or a horizontal magnetic antenna.

The second major element is the preamplifier, which performs initial signal conditioning and amplification. To reduce signal attenuation, the preamplifier is located directly on the structure of the antenna.

Finally, the line receiver filters and digitizes the analog VLF signals. The line receiver consists of a motherboard, which performs the signal processing, an electrical power system (EPS) board, a data acquisition board (DAQ), and a single-board computer (SBC).

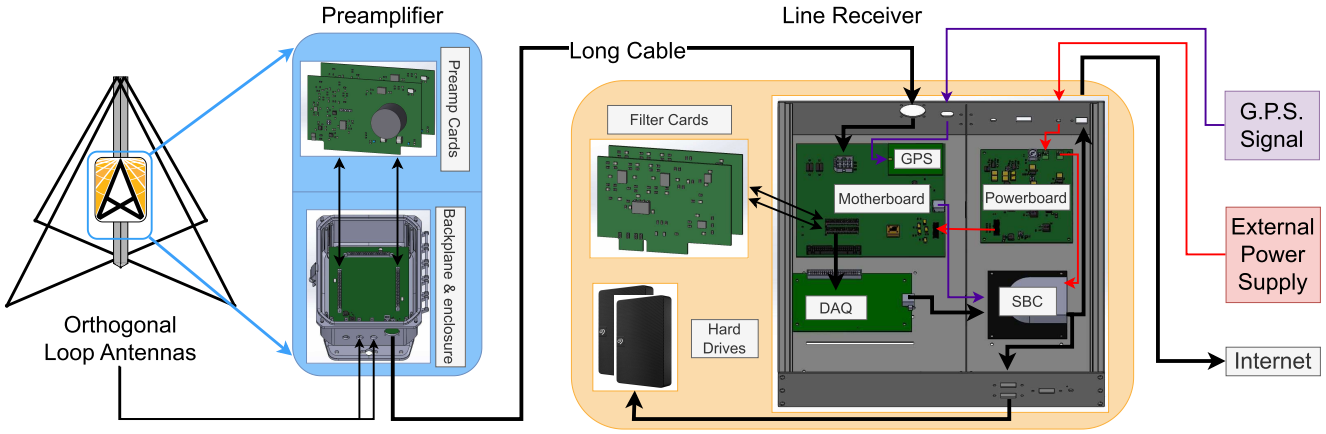

Fig. 1. Functional block diagram of the AVID receiver. The signal is received from the loop antennas in the *XZ* and *YZ* planes, amplified via the preamp (shown on the antenna mounting structure), sent through a long cable to a line receiver set up indoors, and filtered, digitized, timestamped with GPS, and stored.

When identifying the possible deployment locations of the AVID receivers, it is important to note that noise is commonly induced by many buildings, which run power at 60 Hz in North America. To receive signals isolated from electromagnetic interference (EMI), the antennas are often deployed hundreds of meters away from the nearest building. The preamplifier remains close to the antenna to perform amplification at the site of minimal noise. The amplified signal is then sent via a long, shielded cable to the line receiver situated indoors. The line receiver uses a GPS-synchronized sample clock to ensure accurately timestamped data, with sampling precision of about 20 ns [64].

A. Antenna Characteristics

As described in [61] and [62], the desired antenna characteristics include a resistance $R_a = 1\ \Omega$ and inductance $L_a = 0.5$–1.0 mH. These two values can be maintained for different antenna sizes by constraining the geometry to a few basic shapes (right isosceles triangle, square, and circle) and using standard gauges of copper wire, leading to a number of possible antenna designs with different sensitivity and gain. The most common antenna sizes are summarized in Table 1 of [62]. For most of the AVID receiver sites, we use a right isosceles triangle with a base (hypotenuse) of 2.62 m, using 12 turns of 16 AWG copper wire. In one case, due to the proximity to a VLF transmitter, a less sensitive square antenna with 0.16-m base and 47 turns of 20 AWG copper wire was used instead. In general, larger antennas are more sensitive (i.e., have a lower noise floor). However, as the antenna size increases, so too does the complexity of supporting and securing that antenna. The 2.62-m triangular antenna is sufficiently sensitive to measure the narrowband signals of interest for this study at distances of less than 3000 km from the source.

Directly from Faraday's law, the electromotive force (EMF, V) induced by an air-core loop antenna is given by

$$V = \omega NAB \tag{1}$$

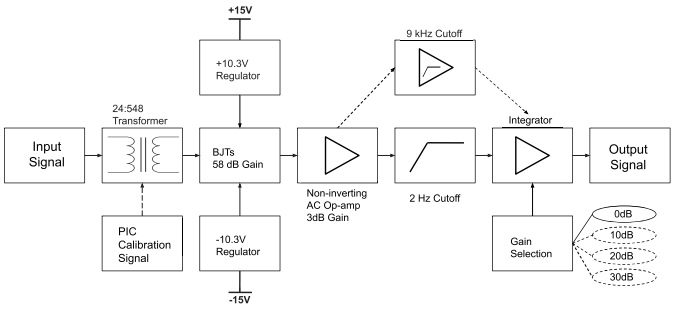

Fig. 2. Block diagram of each preamplifier card. The signal is first passed through an impedance-matching transformer, followed by amplification through a stage of BJTs with a 58-dB gain. The first op-amp amplifies the signal with a 3-dB gain. After the first op-amp, a series of jumpers selects between a variety of application-specific options for frequency cutoff and additional gain.

where $\omega = 2\pi f$ is the wave frequency, N is the number of turns, A is the area of the loop, and B is the magnetic flux density. Using this equation, we can calculate that for a 25-kHz signal with a ~1-pT amplitude (typical of observed VLF transmitter amplitudes at our observation sites), the induced EMF on the 2.62-m base antenna is only 3.2 μV. This underscores the need for signal amplification before transmitting the signal any appreciable distance from the antenna.

B. Low-Noise Amplifier

The antennas typically detect electromagnetic fields in the range of fT to pT, corresponding to voltages in the range of nanovolt–microvolt, so the signal must be amplified before being transmitted through our long cable to the line receiver [61]. Signal amplification is achieved using a low-noise amplifier (LNA), housed on a preamplifier card, for each antenna separately. Each antenna is connected to the preamplifier backplane, which has a preamplifier card for each channel. Fig. 2 shows a block diagram of a preamplifier card, including amplification through the LNA. Before amplification, the input

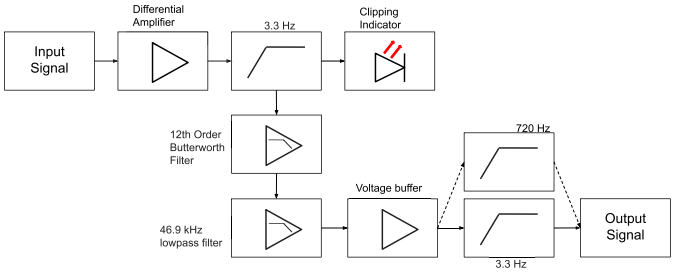

Fig. 3. Simplified version of the filter cards. The signal from the preamplifier travels through a differential amplifier and a 3.3-Hz passive 1st-order high-pass filter, followed by a 12th-order Butterworth filter with a 46.9-kHz cutoff. After the 12th-order filter is a voltage buffer and an optional 720-Hz passive 1st-order high pass.

signal is impedance-matched to the LNA using a custom transformer. This process is described in detail in [65] and [66] and summarized in [62].

The AVID receiver uses a 24:548 ratio transformer, wound in bifilar to have good common-mode rejection. A shield is used between the primary and secondary to reduce electrostatic coupling between the loops. To mitigate the effects of ambient magnetic fields, a pot-core is used. This allows the transformer to have good noise performance and a flat frequency response across the VLF range. In this configuration, the 24-turn side of the transformer faces the antenna signal and serves as the primary.

After the transformer is a series of bipolar common-base circuits that serve as the LNA. This noninverting signal amplifier, where the input and output signals are in phase, has a high gain characteristic. Common-base circuits also have good noise performance and low impedance, so they are preferable to an equivalent circuit designed with operational amplifiers (op-amps) [65]. The preamplifier card has seven such circuits, resulting in a gain of ~58 dB.

The common-base circuit precedes an op-amp configured as a noninverting amplifier with a 3-dB gain under normal operations. However, the circuit can be modified with jumpers to either include frequency compensation with a 3-dB loss or turn on a 9-kHz cutoff, which acts as a filter for the incoming signal, as shown in Fig. 2. The op-amp circuit was modeled to match the input impedance of the common-base circuits. The final stage of the LNA is a noninverting op-amp with gain selections of 0, 10, 20, or 30, with 0 dB being the default option. While higher gain allows for fainter signals to be picked up, it reduces the overall dynamic range of the full system, so in most cases, 0 or 10 dB is the most appropriate choice [61].

C. Analog Filtering

After the LNA amplifies VLF signals, those signals are carried via a long cable, typically 50–150 m long, to the motherboard inside the line receiver. The motherboard hosts a set of filter cards that perform additional signal conditioning on each channel. These cards, sharing heritage with [61], filter with a passband of 3.3–46.9 kHz using a combination of passive and active filters, as seen in Fig. 3.

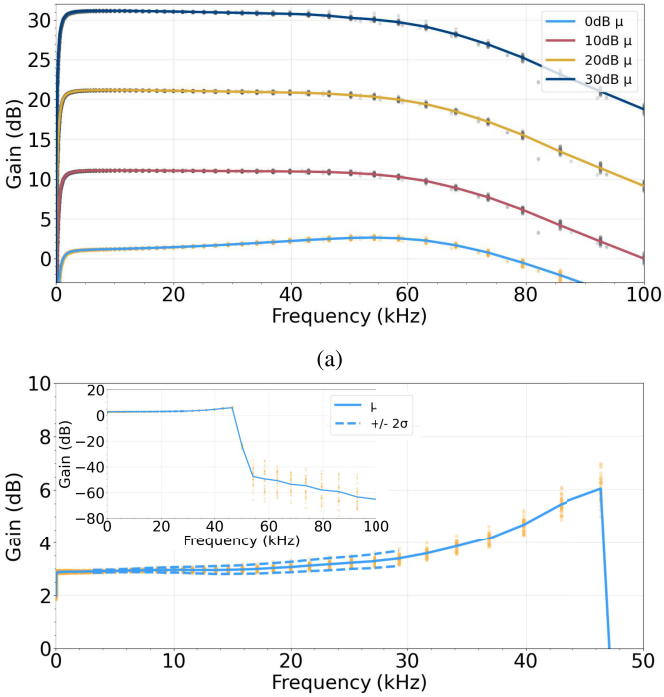

Fig. 4. FRAs of preamplifier cards and filter cards. Each orange dot is the measured gain at that frequency for an individual card. For (a) and (b), μ of all measurements is shown by the solid lines. (b) $\pm 2\sigma$ bounds for 3–30 kHz. The inset of (b) shows an extended frequency range out to 100 kHz and attenuation from −80 to 20 dB.

The signal initially travels through a differential amplifier, followed by a 3.3-Hz passive 1st-order high-pass filter. If the signal amplitude is outside the range from −3 to +3 V, an LED on the motherboard will turn on to indicate clipping in the rest of the circuit. These LEDs precede a 12th-order low-pass Butterworth filter at 46.9 kHz, described in [61], which filters with a cutoff frequency close to 50 kHz such that the NSC VLF transmitter at 45.9 kHz is included in the passband.

After the Butterworth filter, an op-amp doubles as a 46.9-kHz active low-pass filter and a voltage buffer. Before the signal is output from the filter card back to the motherboard, there is an optional 1st-order 720-Hz passive high-pass filter in case the receiver is deployed in an area with significant low-frequency (e.g., power line) noise.

The motherboard then sends the signal from both channels to an off-the-shelf DAQ (DAQ, National Instruments NIDAQ 6211). The DAQ samples each channel simultaneously at 100 kHz, where the sampling frequency is controlled by the GPS receiver clock. This sampling rate gives the system a Nyquist frequency of 50 kHz. The sharp cutoff created by the 12th-order filter, seen in Fig. 4(b), ensures minimal aliasing of signals above 50 kHz.

D. Timing

The AWESOME receiver in [61] uses a custom timing circuit to control the sample clock and reference it to GPS time. In a significant design change, the AVID receiver takes advantage of recent advances in commercially available

GPS-disciplined oscillators. This greatly simplifies the electronics design of AVID's motherboard, relying instead on the accuracy of the user-configurable time pulse from the u-blox LEA M8T GPS module housed on a Synergy Systems SSR-M8T daughter board. This daughter board maintains the legacy communications interface used in the Motorola GPS modules used in the AWESOME receivers, allowing the AVID receiver to pull both software and hardware heritage from AWESOME with small modifications. This GPS module provides both a 1-pulse-per-second and user-configurable time pulse between 0.25 Hz and 10 MHz with a pulse accuracy of ≤20 ns [64]. In the case of the AVID receiver, this is configured to 100 kHz and serves as the sample clock fed directly into the DAQ for data digitization.

E. Power Delivery

In a departure from the previous AWESOME receivers, a new EPS board was designed for these receivers. All system voltages are generated on this separate EPS board, which takes a 19-V dc input. This input voltage is generated with a commercial-of-the-shelf (COTS) 110/220-V ac to 19-V dc converter. We use a low-noise medical-grade laptop power supply for this purpose, selecting a device with a switching frequency well above 100 kHz to avoid switching noise in the frequency band of interest.

This 19-V dc input power is initially filtered using a 2nd-order damped LC low-pass filter with a cutoff at 15.9 kHz. For further conversion, there are several buck converters for the different dc voltage rails. The buck converters were chosen with switching frequencies at 2 MHz (+7, −7, and −17 V), 1.2 MHz (3.3 V), and 500 kHz (+17 V) all well above the frequency range of interest. After each buck converter, there is a 2nd-order LC filter and a low-dropout regulator (LDO) with an additional voltage drop of 2 V to generate the system dc voltages of +/−15 and +/−5 V.

The 3.3-V rail is only used for digital components and therefore does not require significant filtering or smoothing; this voltage is thus directly provided by its own buck converter.

Finally, to further mitigate any noise from the power electronics, the EPS board is spatially separated from the analog electronics and is fully enclosed within a metal structure to reduce EMI.

F. Software and Data Processing

A custom data acquisition software, originally developed in [61], has been updated for this project. A bulk overhaul of the software from Python 2.7 to Python 3.10 was completed. Advances in multithreading hardware and software schedulers allow different DAQ modules to be pushed into their own threads. The modules now run with an optimized prioritization scheme to ensure that data collection, processing, and time synchronization are run at a higher priority than saving to files. This has the effect of reducing conflicts of computer resources that can lead to software interruption. In addition, the DAQ software has a robust set of checks and ability to self-restart in the event of a failure. On a three-day test period, these software improvements led to a 99% uptime of the DAQ software.

IV. Receiver Performance

Frequency response analyses (FRAs) were performed on all 35 manufactured preamplifier cards and 32 manufactured filter cards. This characterization was conducted over a frequency range of 10 Hz–10 MHz with a sampling of 30 samples per decade. Fig. 4(a) shows the FRAs for all four gain options on the preamplifier cards along with the mean frequency response for each gain option.

Similarly, Fig. 4(b) shows the frequency response of all 32 manufactured filter cards, highlighting the mean response as well as $\pm 2\sigma$ for the VLF frequency band (3–30 kHz). As signal frequencies approach the sharp cutoff of the 12th-order Butterworth filter at 46.9 kHz, they show both larger variance and greater gain than the behavior below 30 kHz. While this curve is not flat enough to assume a constant value across the whole frequency range, measurements of this frequency-dependent behavior as deployed in a receiver system allow for the data to be calibrated across the passband.

A. System Calibration

Each preamplifier card uses a PIC12F629 microcontroller to produce a comb signal that can be enabled to perform calibration. The technique of generating and using a comb signal for measuring the frequency response of a system is described in detail in [67] and is similar to how [61] calibrated the AWESOME receivers; however, a discussion of this methodology is included as follows.

Using a linear feedback shift register (LFSR) (see [68] for more detail), a pseudorandom waveform can be generated. In this application, a maximal length sequence (MLS) is chosen such that the sequence length of the shift register is $m = 2^n - 1$. The use of an MLS gives the autocorrelation function

$$R(i) \equiv \frac{1}{m} \sum_{k=0}^{m-1} a_0(k)\, a_0(i-k) \tag{2}$$

which is importantly two-valued, peaking at zero phase. When such an MLS LFSR is implemented from a waveform that oscillates between $-V_p$ and $+V_p$, the rms voltage of the spectral component of a given harmonic frequency is

$$V(0) = \frac{V_p}{m} \tag{3}$$

$$\text{and} \quad V(kf_0) = V_p \frac{\sqrt{2}\,(m+1)^{\frac{1}{2}}}{m} \operatorname{sinc}(k/m), \quad k = 1, 2 \ldots, \tag{4}$$

where $f_0 = f_c/m$ is the sequence repetition rate for a clocked signal of frequency fc. $V(0)$, a small dc voltage, can be ignored in this application as the PIC is capacitively coupled to the signal chain.

The AVID receivers were designed with a 16.384-MHz oscillator. This clock frequency is then divided by four for the internal microprocessor clock and then divided by the cycle time for a shift register, which is eight instructions. For the comb, this arrangement yields $f_c = 512$ kHz. A sequence length of $m = 2047$ was chosen, giving a frequency spacing of 250.1221 Hz between each peak of the comb. This comb signal

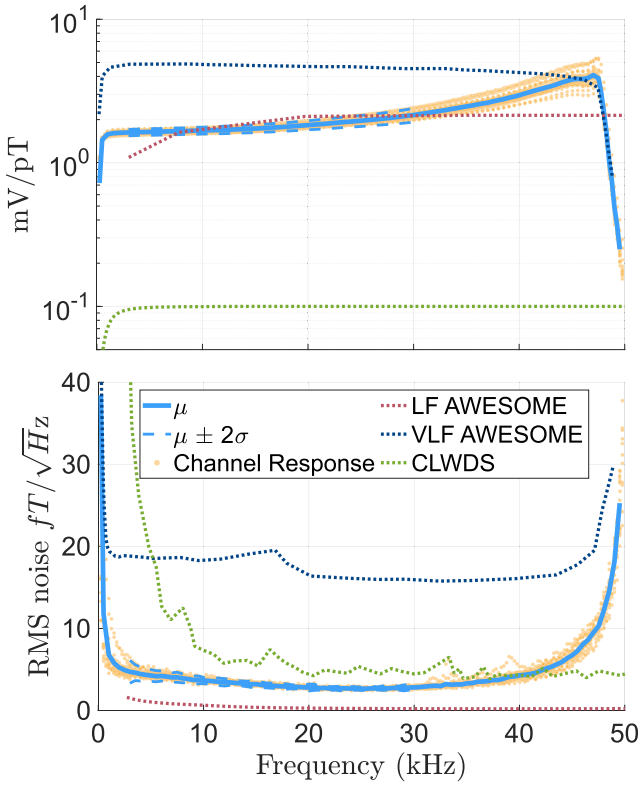

Fig. 5. (Top) Calibrated frequency response and (bottom) noise response for both channels of all 11 systems deployed. The individual measurements are plotted in orange with the $\mu \pm 2\sigma$ highlighted in blue. The performance of three similar instruments is reproduced as well: the original VLF AWESOME [61] (0.8–47 kHz), the extended range LF AWESOME [62] (0.5–470 kHz), and the CLWDS [60] (10–300 kHz).

has a maximum amplitude difference between the 250.1221 and 49774.30 Hz of <0.15 dB (98.44% uniformity).

Measurement of this signal by the DAQ provides a means to quantify the frequency response of each channel of a fully deployed system. Further accounting for the antenna characteristics through their Faraday's law response allows each channel to have a frequency-dependent amplitude response in millivolts recorded at the DAQ per pT in input magnetic flux amplitude. For the AVID project, 11 receivers have been deployed, giving 22 channels that have been calibrated in the field in this way. Fig. 5 shows the results of this calibration along with the frequency responses of other similar instruments [60], [61], [62]. Note that while the system design is identical for each site, the cable that carries the signals from the preamplifier to the line receiver varies between 10 and 150 m long at different sites, resulting in slight differences in the signal loss along the cable. In the 3-30-kHz range, the 2σ bounds follow the mean response within 0.2448 mV/pT. At 20 kHz, the mean response is 1.831 ± 0.1325 mV/pT.

B. Noise Floor

Having carefully calibrated each receiver channel for the 11 deployed instruments, an input-referenced noise floor was calculated for each channel using data collected without antennas connected. The data recorded at the DAQ are representative of the noise intrinsic in the system as well as any electromagnetic noise that couples from an indoor, on-grid environment. By using the same antenna properties as the system would normally have, the noise referenced to the antenna can be calculated in fT/(Hz)$^{1/2}$. Fig. 5 displays these results with the mean response and $\pm 2\sigma$ highlighted for all 11 deployed receivers in their final environment. For the region of primary interest (3–30 kHz), the AVID receivers have an operational noise floor lower than 4.7 ± 1.4 fT/(Hz)$^{1/2}$ with a noise floor of 2.8 ± 0.4 fT/(Hz)$^{1/2}$ at 20 kHz.

V. Applications in the Array for VLF Imaging of the D-Region

Historically, VLF subionospheric remote sensing has been used to draw conclusions about the average state of the D-region ionosphere across specific transmit–receive great circle paths (GCPs) (see [13], [35], [69], [70]). While this allows for continuous time-resolution measurements of the D-region ionosphere along a GCP, it limits the ability to gain insights into the spatial extent of disturbances along the path.

Recent efforts have focused on aggregating measurements from multiple sources and/or receivers to better understand the spatial scale of ionospheric disturbances within the D-region. The earliest of these was the Holographic Array for Ionospheric Lightning (HAIL) research, which applied the idea of strip holographic imaging inside of the EI waveguide using a line of seven to nine receivers spaced ~ 50 km apart to image small scale (<100 km) disturbances in the D-region [17], [18], [19], [20], [71]. More recently, the South America VLF NETwork (SAVNET), consisting of seven VLF receivers, was deployed to study solar effects on the D-region ionosphere as well as advance our understanding of the South American Magnetic Anomaly [21], [22]. Around the same time, the Antarctic–Arctic radiation-belt (dynamic) deposition-VLF atmospheric research Konsortium network (AARDVARK) was deployed globally, focusing on high-latitude connections between the ionosphere, magnetosphere, and solar protons [27]. While all of these networks focus on the measurement of narrowband VLF transmitter signals, in the last decade, a parallel approach was introduced, making use of broadband sferic measurements in a tomographic approach to imaging the D-region ionosphere [23], [26]. Contrasting that, advanced methods have been devised for estimating mesoscale features in the D-region ionosphere from an array of measurements that fully enclose a region [72], [73], [74]. It is this final method that informed the design of our array of VLF receivers.

Fig. 6 shows the array for VLF imaging of the D-region (AVID), which consists primarily of receivers described in Sections III and IV. AVID's multiple and overlapping paths enable spatial analyses to be undertaken from VLF measurements [72], [73], [74]. AVID is comprised of 11 VLF receivers ranging from 470 to 2860 km from the Naval transmitters in Washington (NLK, 24.8 kHz) and North Dakota (NML, 25.2 kHz). Using these two transmitters, 22 GCPs are created. The area bounded by AVID's network of GCPs spans ~ 2500 km in longitude and ~ 1500 km in latitude, covering roughly $L = 3$ to $L = 7$ in geomagnetic coordinates and ~ 2.5 h of local time. An additional two VLF receivers are located 15.3 km (~ $1.3\lambda_{\text{NLK}}$) and 3.7 km (~ $0.3\lambda_{\text{NML}}$) away from

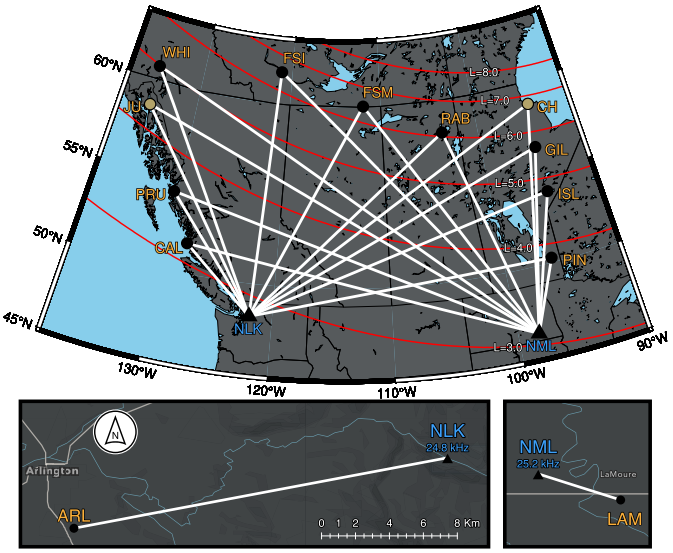

Fig. 6. (Top) Map of the 11 VLF receivers (black dots) and two VLF transmitters (black triangles) that together create the 22 transmit–receive paths across western Canada. Gold dots (JU and CH) note receivers operated by the Low Frequency Radio Group at Georgia Institute of Technology. Red lines indicate magnetic L-shells. (Bottom) insets showing the VLF receivers placed near the NLK and NML transmitters and their relevant propagation paths.

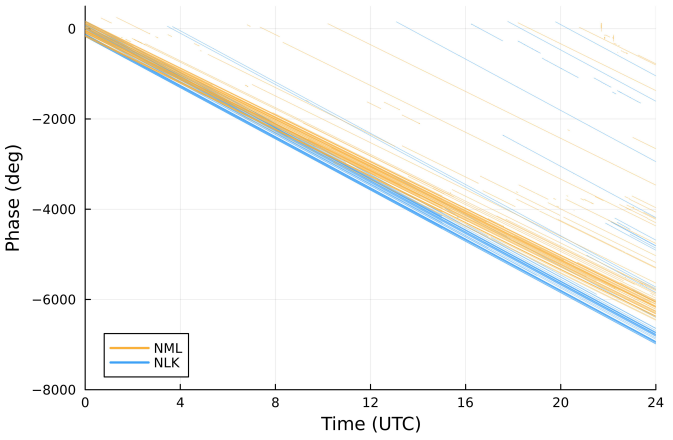

Fig. 7. Three months of measured phase angle over time plotted by day for the NLK transmitter (blue) measured at the ARL VLF receiver and the NML transmitter (orange) measured at the LAM VLF receiver.

NLK and NML, respectively, to monitor the transmitted phase and power, which are not otherwise publicly available. The locations of these two receivers are shown in the lower two panels of Fig. 6.

A. Transmitter Characterization

1) Phase Drift: Phase changes along a VLF GCP have long been correlated directly with ionospheric changes (see [34]) and are, for certain events, more important than amplitude changes, as EI waveguide modeling is not always necessary to draw conclusions from phase data (see [31], [75]).

Recent studies have encountered issues with phase measurements from several of the major VLF transmitters ([33], [76], [77]). Presented by some authors as "unstable," Gu et al. [77] appeared to show in their Figs. 2 and 3 that these

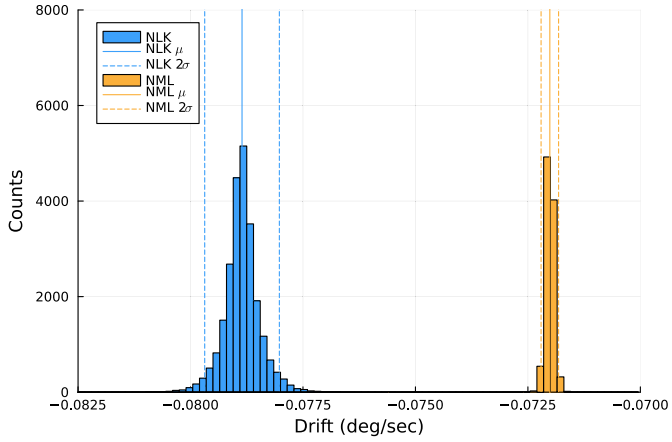

Fig. 8. Histograms of the drifts as calculated from the linear regressions of the NLK (blue) and NML (orange) transmitters. Mean (μ) and 2σ bounds are shown for both and are $-0.07886°/s \pm 0.00083°/s$ and $-0.07201°/s \pm 0.00019°/s$, respectively.

transmitters exhibit a steady drift in phase while transmitting. This is observed by the VLF receivers in AVID as well. Crucially, however, the ARL and LAM receivers are located well within 60 km, less than the typical effective height for the D-region ionosphere, from the NLK and NML transmitters, respectively, which allows them to capture a clear picture of this drifting phase without the effects of the dynamic ionosphere overlaid. ARL was deployed on April 1, 2023, while LAM was deployed on May 21, 2024. Fig. 7 shows the daily measured phase for three consecutive months of both LAM and ARL measurements. From this figure, it is clear that the bulk behavior for both the NLK and NML transmitters is a steady negative drift in the phase transmitted. It is also clear that each transmitter has a different rate of drift in the transmitted phase. For work within the AVID array and beyond in general VLF studies, characterization of this bulk drift allows phase data to be corrected and made usable for analysis.

One central challenge to characterizing the phase drift of these transmitters is simply that the transmitter and/or the receiver can turn off sporadically. Often, only for a few seconds, these gaps in data are present on most days. To circumvent these gaps, all available data were split into windows of 30 min of continuous data. Then, a linear regression was performed on each window (n = 1800 s) of data.

From each regression, the slope parameter was extracted. For both NLK and NML, the channel of the observing VLF receiver most closely aligned with the direction of propagation from the transmitter was found to yield more consistent drift rates and so is exclusively presented here. Fig 8 shows a histogram of both NLK and NML drift rates as calculated through these linear regressions, with visual indications of the mean and $\pm 2\sigma$. This analysis results in a stable drift of $-0.07886°/s \pm 0.00083°/s$ for NLK and $-0.07201°/s \pm 0.00019°/s$ for NML.

Fig. 9 shows the application of the phase drift correction procedure for the FSI receiver tracking the NLK transmitter. This transmitter–receiver pair has a path length of 1510 km.

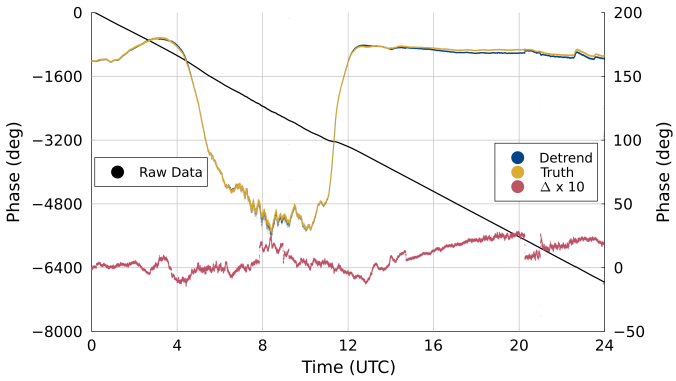

Fig. 9. NLK phase data collected at AVID station FSI. The raw phase data showing drift (black, left axis) underscores the need for phase correction. The data detrended using a slope of –0.07886°/s (blue, right axis) are compared to the true phase change along the path as calculated from the reference measurements at ARL (orange, right axis). The difference between the detrended and true phases is magnified by 10× (red, right axis), showing less than 3° disagreement across this 24-h example.

The uncorrected phase data, in black, show that the drift dominates over the diurnal sunrise/sunset effects on phase for this path, making it nearly impossible to discern any geophysical effects along this path. A "true" phase, in orange, is calculated as the difference between the FSI phase measurement and the phase measured at ARL, 15 km from NLK. This is represented by (5)

$$\phi_{\text{truth}}(t) = \phi_{\text{FSI}}(t) - \phi_{\text{ARL}}(t) \tag{5}$$

$$\phi_{\text{detrend}}(t) = \phi_{\text{FSI}}(t) - (\mu t). \tag{6}$$

Separately, a detrended phase, in blue, is calculated without the use of a reference measurement, described in (6), where μ is the average phase drift for the transmitter as characterized in Fig. 8. The difference between the detrended phase and the true phase, in red magnified by a factor of 10, shows that for this path and day, the detrended phase is always within 3° of the true phase. When possible, a reference phase should be used to capture small phase shifts from the transmitter; however, detrending the drifting phase with the average drift, as shown here, closely matches the true phase change along a path.

2) Transmitted Power: Operating receivers within an ionospheric height of the transmitters allows the relative transmitted power to be tracked. Fig. 10 shows the magnetic field amplitude of the nearby transmitter signal over the current lifetime of the ARL and LAM receivers. For this figure, dots near zero have been enlarged to emphasize the times in which the transmitter was offline, while times where there is no corresponding magnetic field measurement are times for which the relevant receiver was offline. Note that in this case, following the derivation in [78, pp. 293–299], the amplitude of NML is scaled by

$$B_{\text{scaled}} = B_{\text{measured}} \frac{d_{\text{ARL}}^{-2} + k_0/d_{\text{ARL}}}{d_{\text{LAM}}^{-2} + k_0/d_{\text{LAM}}} \tag{7}$$

where d_{ARL} is the distance from NLK to ARL, d_{LAM} is the distance from NML to LAM, and k_0 is the wavenumber for

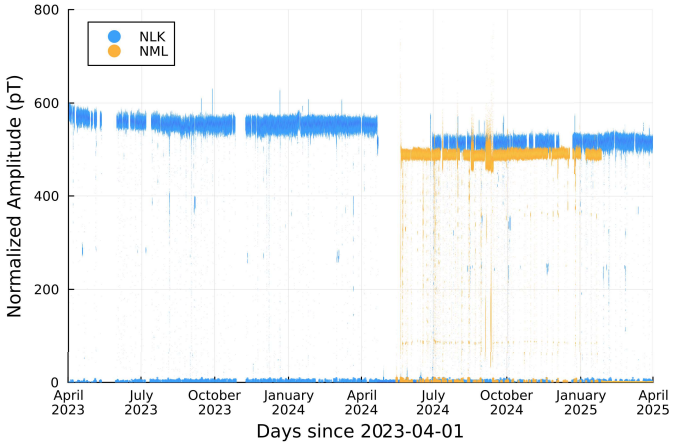

Fig. 10. Received signal amplitude in pT for the NLK (blue) and NML (orange) transmitters at ARL and LAM, respectively. NML signal amplitude has been scaled by distance to match that of NLK at 15.3 km. Points near zero are enlarged to show times when each transmitter was offline.

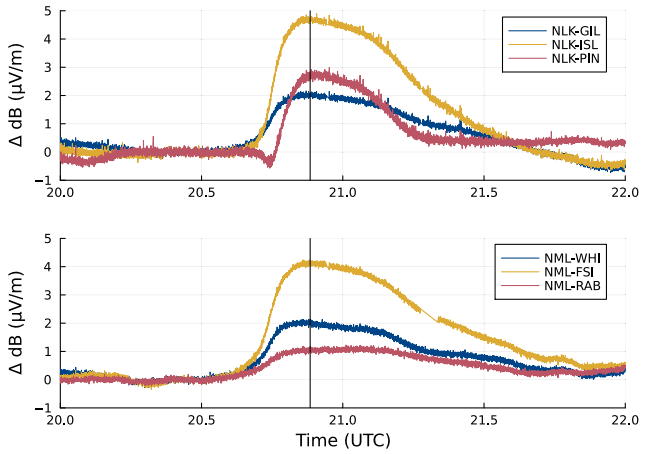

Fig. 11. Normalized amplitude data for selected paths from (top) NLK and (bottom) NML for a 2-h window that includes an M7.2 solar flare. The vertical black line denotes the time that the middle panel of Fig. 12 shows.

NML transmitting at 25.2 kHz. Scaling in this manner normalizes NML's signal strength to that which would be measured at the same distance as ARL measures NLK, allowing a direct comparison between the NML and NLK signal strengths.

From this figure, it is clear that the transmitters do not always operate with the same power envelope. In particular, NLK can be seen to drop ~7% after three months of downtime between April and July 2024. These operational changes must be accounted for in longitudinal studies so as not to erroneously be confused with ionospheric or solar cycle variation. AVID's ability to track these power changes allows for these and future transmitter power changes to be incorporated into studies that span extended observational periods.

B. First Results: Response to Solar Flare

In this section, we present data from a recent solar flare in order to demonstrate the capability of the AVID system. During a solar flare, the normally dominant source of ionization in the D-region, solar Lyman-α radiation, gets quickly eclipsed by X-rays [1], [79]. On October 30, 2024, starting at

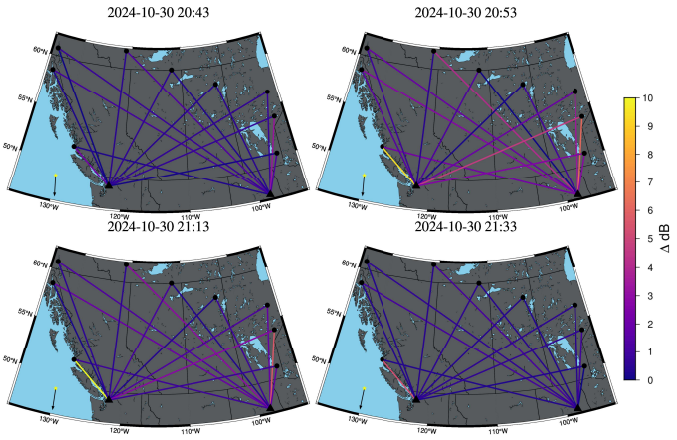

Fig. 12. Four panels, 10 min apart during the rise and peak, and then 20 min apart during the recovery of the D-region's response to an M7.2 solar flare. The arrow in the bottom left of each panel indicates direction toward the subsolar point. Each path's color indicates the |Δ dB μV/m| from a pre-flare baseline. The second panel matches in time with the vertical black line in Fig. 11.

20:29 UTC, an M7.2 flare was identified by the GOES XRS instrument. Fig. 11 shows the examples of VLF amplitude data for three NLK paths and three NML paths. Each path was normalized using a 5-min average before the detection of the flare by GOES in order to find a reference amplitude (Δ dB = 0 in the figure). The plot then shows the change in signal amplitude (dB μV/m) as the X-ray flux from the flare rapidly ionizes the D-region and then gradually fades.

While the temporal signature of the flare is similar for most of the paths shown, NLK-PIN in particular has an unusual response, dropping below 0 dB before rising like the rest of the paths. This behavior is likely caused by changes in the waveguide mode interference pattern during the flare and highlights one of the challenges of interpreting subionospheric VLF signals using individual transmitter–receiver pairs.

For this event, a total of 18 paths captured the solar flare (three receivers were not operational). Fig. 12 visualizes the change in signal amplitude for each path at specific times during the flare using the color of each path to represent the |Δ dB μV/m| from the pre-flare activity. The middle panel in Fig. 12 is the same time as the vertical line in Fig. 11, near the peak of the flare. For this event, the subsolar point was at ~ 14° S and progressed from ~ 131° W to ~ 147° W over the time of the event; the direction to the subsolar point is indicated in each panel with an arrow in the lower left corner.

In general, the southernmost AVID paths respond to the flare more than the northernmost paths, consistent with the subsolar point being in the southern hemisphere. Despite possible complexities with the modal structure changing in the EI waveguide as the D-region responds to an increase in ionization, AVID shows a reasonably smooth response to this flare in measured VLF amplitude, and the response appears to vary smoothly with solar zenith angle (SZA). Future work will expand on this analysis through the use of simulation tools, such as the LongwaveModePropagator (LMP) [73], [74], [80] to quantify the impact of this and other flares on the D-region ionization across this mesoscale region of space.

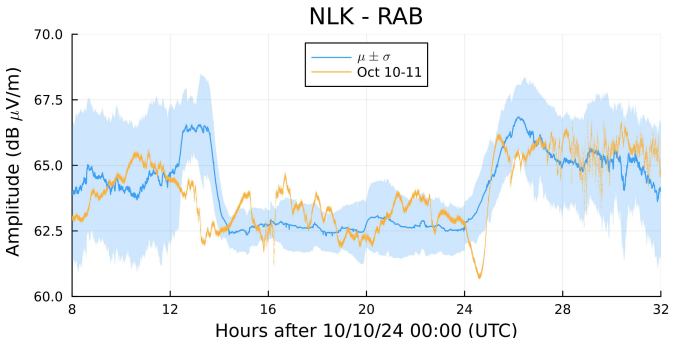

Fig. 13. "Quiet day curve" for the NLK-RAB path is shown in blue as the average of ±20 geomagnetically quiet days around October 10. ±σ from the mean shown in the shaded region. Orange is the NLK-RAB path's amplitude response versus time.

C. First Results: October 10 and 11, 2024, Geomagnetic Storm

As discussed in the introduction, AVID was designed to measure the D-region response to geomagnetic activity through EPP. AVID was operational during the October 10 to 11, 2024, geomagnetic storm, providing our first observation of geomagnetic activity with the complete array. This storm peaked at Dst = −333 nT and was classified by the National Oceanic and Atmospheric Administration's Space Weather Prediction Center (NOAA SWPC) as a G4 storm. During the onset of a geomagnetic storm, radiation-belt particles are depleted, many of which are lost in the atmosphere as EPP [81], [82]. EPP can cause an enhancement to D-region densities if the electrons have energies greater than 30 keV [1], [8]. Following the initial dropout of energetic particles in a storm, studies of wave–particle interactions in the Earth's magnetosphere have shown that chorus-driven precipitation primarily occurs on the dawn side of the Earth [83], [84]. Immediately preceding storm onset, AVID was in the pre-dawn sector.

To assess signatures of EPP in AVID data, background quiet days are calculated for each path. A time range of ±20 days from October 10, 2024, was used to compute the average VLF signal amplitude measured at each timestep. Times were excluded if the Dst index was at or below −30 nT, indicating minor geomagnetic storm conditions were present [85], [86]. Also excluded were times in which SWPC, using the GOES XRS instrument, detected a solar flare with peak magnitude larger than M1.0 and any part of the specific path being considered had an SZA less than 90°, indicating that some part of the path was illuminated by the sun.

Fig. 13 shows an example of this quiet-day analysis as applied to the NLK to RAB path. Note that sunrise occurs around 13–14 UTC and sunset around 01–02 UTC (25–26 on this figure). The average "quiet-day curve" is shown in blue with 1σ bounds shown in the shaded region. The 24 h period, including storm onset, main phase, and recovery, is shown in the orange line. Deviations from the quiet day are indicative of a disturbed D-region along this path. Of particular note for this early study is the time between 12 and 14 UTC, directly before dawn and during sunrise, when the amplitude on this path deviates by ~4 dB μV/m.

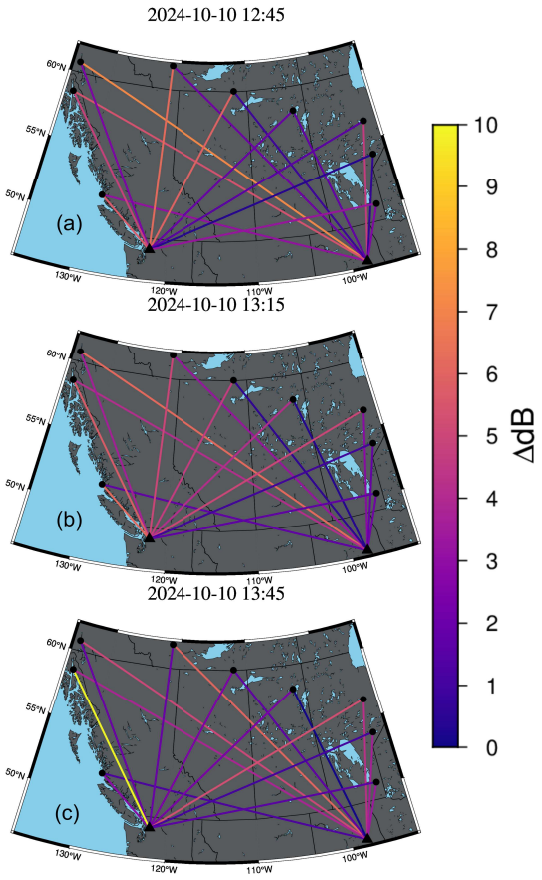

Fig. 14. Three panels, each 30 min apart, showing AVID's measurement of the D-region's response to the onset of the October 10 and 11 geomagnetic storm.

This process was repeated for each path. Fig. 14 shows three instances in time during the pre-dawn period before the onset of the October 10 and 11 geomagnetic storm when AVID had 18 operational paths. In the first panel, a clear disturbance can be localized primarily over the intersection of the NLK-FSM and NML-WHI paths. The second panel, 30 min later, shows the same disturbance fading and spreading out eastward. In the final panel, a disturbance can be localized to the center of the array and a second disturbance appears to exist at the eastern-most edge, where the NML-PIN, NML-GIL, and NML-ISL paths show significant response.

This possible second disturbance becomes complicated to interpret beyond the qualitative manner discussed thus far. Modal interference of the VLF signals in the EI waveguide limits this type of analysis, which relies on deviations from previous known behavior. While these observations show how the AVID array can be used to spatially locate D-region disturbances, it is clear that more advanced analysis and inversion techniques are needed to extract quantitative spatial information, as well as quantitative estimates of the D-region disturbance in terms of the changes in electron density and reflection height. Future work will utilize methods such as the local ensemble transform Kalman filter (LETKF) developed in [72] and [74] to study EPP in more detail.

VI. Conclusion

This article presents the AVID VLF receiver and discusses the calibration and characterization of each receiver. Statistical bounds are given for the 3–30-kHz range based on 11 field-deployed receivers giving a total of 22 analog channels from which we draw characterization data. The array for VLF imaging of the D-region is also presented, covering a mesoscale region of Canada ~2500 × ~1500 km, and spanning L-shells from roughly $L = 3$ to $L = 7$. VLF data from the ARL and LAM receivers were used to characterize the phase drift rates of the NLK and NML VLF transmitters ($-0.07886°/s \pm 0.00083°/s$ and $-0.07201°/s \pm 0.00019°/s$, respectively). These same receivers show that the power envelope used by the transmitters is not always constant, with the NLK transmitter in particular having ~7% reduced power after July 1, 2024.

AVID data were used to look first at the October 30, 2024, M7.2 solar flare. This showed, qualitatively, a peak response that varied with SZA and a smooth rise in amplitude response followed by an extended decay. Finally, AVID data for the onset of the October 10 and 11, 2024, G4 geomagnetic storm were presented. During the pre-dawn onset of the storm, AVID saw clear disturbances that could be spatially localized and tracked over time, albeit qualitatively in this preliminary analysis.

The D-region ionosphere continues to be a region that is challenging to measure, but simultaneously crucial to understand in its coupling to the magnetosphere above and the neutral atmosphere below [1], [2], [3], [4], [5], [13]. AVID, as a cohesive geophysical observatory, presents the unique opportunity to identify and track mesoscale phenomena in the D-region ionosphere. The characterization results reported here, along with the first results of two geomagnetically active events, lay the groundwork for a suite of new studies to follow, which will quantify the spatial and temporal extent and evolution of solar flares, EPP events, and other D-region disturbances.

References

[1] M. C. Kelley, *The Earth's Ionosphere: Plasma Physics and Electrodynamics*. New York, NY, USA: Academic, 2009.

[2] M. V. Codrescu, T. J. Fuller-Rowell, R. G. Roble, and D. S. Evans, "Medium energy particle precipitation influences on the mesosphere and lower thermosphere," *J. Geophys. Res., Space Phys.*, vol. 102, no. A9, pp. 19977–19987, Sep. 1997.

[3] I. A. Mironova et al., "Energetic particle influence on the Earth's atmosphere," *Space Sci. Rev.*, vol. 194, pp. 1–96, Nov. 2015.

[4] D. W. Rusch, J.-C. Gérard, S. Solomon, P. J. Crutzen, and G. C. Reid, "The effect of particle precipitation events on the neutral and ion chemistry of the middle atmosphere—I. Odd nitrogen," *Planet. Space Sci.*, vol. 29, no. 7, pp. 767–774, Jul. 1981.

[5] S. Solomon, D. W. Rusch, J. C. Gérard, G. C. Reid, and P. J. Crutzen, "The effect of particle precipitation events on the neutral and ion chemistry of the middle atmosphere: II. Odd hydrogen," *Planet. Space Sci.*, vol. 29, no. 8, pp. 885–893, Aug. 1981.

[6] C. E. Randall et al., "Simulation of energetic particle precipitation effects during the 2003–2004 Arctic winter," *J. Geophys. Res., Space Phys.*, vol. 120, no. 6, pp. 5035–5048, Jun. 2015.

[7] R. A. Marshall et al., "The AEPEX mission: Imaging energetic particle precipitation in the atmosphere through its bremsstrahlung X-ray signatures," *Adv. Space Res.*, vol. 66, no. 1, pp. 66–82, Jul. 2020.

[8] R. A. Marshall and C. M. Cully, "Atmospheric effects and signatures of high-energy electron precipitation," in *The Dynamic Loss of Earth's Radiation Belts*. Amsterdam, The Netherlands: Elsevier, 2020, pp. 199–255.

[9] M. Friedrich and K. M. Torkar, "FIRI: A semiempirical model of the lower ionosphere," *J. Geophys. Res., Space Phys.*, vol. 106, no. A10, pp. 21409–21418, Oct. 2001.

[10] M. Friedrich, C. Pock, and K. Torkar, "FIRI-2018, an updated empirical model of the lower ionosphere," *J. Geophys. Res., Space Phys.*, vol. 123, no. 8, pp. 6737–6751, Aug. 2018.

[11] Q. Ma et al., "Analysis of electron precipitation and ionospheric density enhancements due to hiss using incoherent scatter radar and Arase observations," *J. Geophys. Res., Space Phys.*, vol. 127, no. 8, 2022, Art. no. e2022JA030545.

[12] D. McKay-Bukowski et al., "Kaira: The kilpisjärvi atmospheric imaging receiver array-system overview and first results," *IEEE Trans. Geosci. Remote Sens.*, vol. 53, no. 3, pp. 1440–1451, Mar. 2014.

[13] U. S. Inan, S. A. Cummer, and R. A. Marshall, "A survey of ELF and VLF research on lightning-ionosphere interactions and causative discharges," *J. Geophys. Res., Space Phys.*, vol. 115, no. 6, pp. 1–21, Jun. 2010.

[14] S. A. Cummer, U. S. Inan, and T. F. Bell, "Ionospheric d region remote sensing using VLF radio atmospherics," *Radio Sci.*, vol. 33, no. 6, pp. 1781–1792, Nov. 1998.

[15] R. A. Marshall and J. B. Snively, "Very low frequency subionospheric remote sensing of thunderstorm-driven acoustic waves in the lower ionosphere," *J. Geophys. Res., Atmos.*, vol. 119, no. 9, pp. 5037–5045, May 2014.

[16] U. S. Inan, F. A. Knifsend, and J. Oh, "Subionospheric VLF 'imaging' of lightning-induced electron precipitation from the magnetosphere," *J. Geophys. Res., Space Phys.*, vol. 95, no. 10, pp. 17217–17231, 1990.

[17] J.-T. Chen, U. S. Inan, and T. F. Bell, "VLF strip holographic imaging of lightning-associated ionospheric disturbances," *Radio Sci.*, vol. 31, no. 2, pp. 335–348, Mar. 1996.

[18] M. P. Johnson, U. S. Inan, S. J. Lev-Tov, and T. F. Bell, "Scattering pattern of lightning-induced ionospheric disturbances associated with early/fast VLF events," *Geophys. Res. Lett.*, vol. 26, no. 15, pp. 2363–2366, Aug. 1999.

[19] W. B. Peter, M. W. Chevalier, and U. S. Inan, "Perturbations of mid-latitude subionospheric VLF signals associated with lower ionospheric disturbances during major geomagnetic storms," *J. Geophys. Res., Space Phys.*, vol. 111, no. A3, pp. 1–14, Mar. 2006.

[20] W. B. Peter and U. S. Inan, "A quantitative comparison of lightning-induced electron precipitation and VLF signal perturbations," *J. Geophys. Res., Space Phys.*, vol. 112, no. A12, pp. 1–20, Dec. 2007.

[21] J.-P. Raulin, P. Correia de Matos David, R. Hadano, A. C. V. Saraiva, E. Correia, and P. Kaufmann, "The South America VLF NETwork (SAVNET)," *Earth, Moon, Planets*, vol. 104, nos. 1–4, pp. 247–261, Apr. 2009.

[22] J. P. Raulin, P. Correia de Matos David, R. Hadano, A. C. V. Saraiva, E. Correia, and P. Kaufmann, "The South America VLF NETwork (SAVNET): Development, installation status, first results," *Geofísica Internacional*, vol. 48, no. 3, pp. 253–261, Jul. 2009.

[23] J. C. McCormick, M. B. Cohen, N. C. Gross, and R. K. Said, "Spatial and temporal ionospheric monitoring using broadband sferic measurements," *J. Geophys. Res., Space Phys.*, vol. 123, no. 4, pp. 3111–3130, Apr. 2018.

[24] J. C. McCormick, "D-region tomography: A technique for ionospheric imaging using lightning generated sferics and inverse modeling," Ph.D. dissertation, Georgia Institute of Technology, Atlanta, GA, USA, 2019.

[25] D. K. Richardson, J. C. McCormick, and M. B. Cohen, "A D-region ionospheric imaging method using sferic-based tomography," *J. Geophys. Res., Space Phys.*, vol. 128, no. 8, p. 2023, Aug. 2023, Art. no. e2023JA031573. [Online]. Available: https://agupubs.onlinelibrary.wiley.com/doi/abs/10.1029/2023JA031573

[26] D. K. Richardson and M. B. Cohen, "Unifying VLF transmitter and sferic modeling efforts via tomography," *J. Geophys. Res., Space Phys.*, vol. 128, no. 11, p. 2023, Nov. 2023, Art. no. e2023JA031989.

[27] M. A. Clilverd et al., "Remote sensing space weather events: Antarctic-Arctic radiation-belt (dynamic) deposition-VLF atmospheric research konsortium network," *Space Weather*, vol. 7, no. 4, pp. 1–15, Apr. 2009.

[28] M. Gołkowski, N. C. Gross, R. C. Moore, B. R. T. Cotts, and M. Mitchell, "Observation of local and conjugate ionospheric perturbations from individual oceanic lightning flashes," *Geophys. Res. Lett.*, vol. 41, no. 2, pp. 273–279, Jan. 2014.

[29] R. A. Marshall and U. S. Inan, "Two-dimensional frequency domain modeling of lightning EMP-induced perturbations to VLF transmitter signals," *J. Geophys. Res., Space Phys.*, vol. 115, no. A6, pp. 1–13, Jun. 2010.

[30] S. A. Cummer, T. F. Bell, U. S. Inan, and D. L. Chenette, "VLF remote sensing of high-energy auroral particle precipitation," *J. Geophys. Res., Space Phys.*, vol. 102, no. A4, pp. 7477–7484, Apr. 1997.

[31] N. C. Gross, M. B. Cohen, R. K. Said, and M. Gołkowski, "Polarization of narrowband VLF transmitter signals as an ionospheric diagnostic," *J. Geophys. Res., Space Phys.*, vol. 123, no. 1, pp. 901–917, Jan. 2018.

[32] S. Maekawa and M. Hayakawa, "A statistical study on the dependence of characteristics of VLF/LF terminator times on the propagation direction," *IEEJ Trans. Fundamentals Mater.*, vol. 126, no. 4, pp. 220–226, 2006.

[33] W. Xu et al., "Measurements and modeling of the responses of VLF transmitter signals to X-class solar flares at the great wall station in Antarctica," *Space Weather*, vol. 21, no. 4, p. 2022, Apr. 2023.

[34] N. R. Thomson, C. J. Rodger, and M. A. Clilverd, "Large solar flares and their ionospheric d region enhancements," *J. Geophys. Res., Space Phys.*, vol. 110, no. A6, pp. 1–10, Jun. 2005.

[35] A. Kumar and S. Kumar, "Solar flare effects on D-region ionosphere using VLF measurements during low- and high-solar activity phases of solar cycle 24," *Earth, Planets Space*, vol. 70, no. 1, pp. 1–14, Dec. 2018.

[36] M. A. Clilverd et al., "Total solar eclipse effects on VLF signals: Observations and modeling," *Radio Sci.*, vol. 36, no. 4, pp. 773–788, Jul. 2001.

[37] M. B. Cohen et al., "The lower ionospheric VLF/LF response to the 2017 great American solar eclipse observed across the continent," *Geophys. Res. Lett.*, vol. 45, no. 8, pp. 3348–3355, Apr. 2018.

[38] W. Xu et al., "VLF measurements and modeling of the D-region response to the 2017 total solar eclipse," *IEEE Trans. Geosci. Remote Sens.*, vol. 57, no. 10, pp. 7613–7622, Oct. 2019.

[39] A. Nina and V. Čadež, "Detection of acoustic-gravity waves in lower ionosphere by VLF radio waves," *Geophys. Res. Lett.*, vol. 40, no. 18, pp. 4803–4807, Sep. 2013.

[40] S. Pal, S. Chakraborty, and S. K. Chakrabarti, "On the use of very low frequency transmitter data for remote sensing of atmospheric gravity and planetary waves," *Adv. Space Res.*, vol. 55, no. 4, pp. 1190–1198, Feb. 2015.

[41] S. Biswas, S. Chowdhury, S. Sasmal, D. Z. Politis, S. M. Potirakis, and M. Hayakawa, "Numerical modelling of sub-ionospheric very low frequency radio signal anomalies during the samos (Greece) earthquake (M = 6.9) on October 30, 2020," *Adv. Space Res.*, vol. 70, no. 5, pp. 1453–1471, Sep. 2022.

[42] M. Hayakawa, *Earthquake Prediction With Radio Techniques*. Hoboken, NJ, USA: Wiley, 2015.

[43] D. Z. Politis, S. Sasmal, M. Hayakawa, H. Haralambous, A. Datta, and S. M. Potirakis, "A six-year (2014–2020) statistical correlation study of VLF terminator time shift with earthquakes in Japan," *Remote Sens.*, vol. 16, no. 22, p. 4162, Nov. 2024.

[44] M. B. Cohen and R. A. Marshall, "ELF/VLF recordings during the 11 March 2011 Japanese Tohoku earthquake," *Geophys. Res. Lett.*, vol. 39, no. 11, pp. 1–5, Jun. 2012.

[45] C. J. Rodger, N. R. Thomson, and R. L. Dowden, "A search for ELF/VLF activity associated with earthquakes using ISIS satellite data," *J. Geophys. Res., Space Phys.*, vol. 101, no. A6, pp. 13369–13378, Jun. 1996.

[46] J. C. McCormick and M. B. Cohen, "A new four-parameter D-region ionospheric model: Inferences from lightning-emitted VLF signals," *J. Geophys. Res., Space Phys.*, vol. 126, no. 12, p. 2021, Dec. 2021.

[47] E. H. Lay and X.-M. Shao, "High temporal and spatial-resolution detection of D-layer fluctuations by using time-domain lightning waveforms," *J. Geophys. Res., Space Phys.*, vol. 116, no. A1, pp. 1–8, Jan. 2011.

[48] R. A. Marshall, "An improved model of the lightning electromagnetic field interaction with the D-region ionosphere," *J. Geophys. Res., Space Phys.*, vol. 117, no. A3, pp. 1–15, Mar. 2012.

[49] U. S. Inan, T. F. Bell, and J. V. Rodriguez, "Heating and ionization of the lower ionosphere by lightning," *Geophys. Res. Lett.*, vol. 18, no. 4, pp. 705–708, Apr. 1991.

[50] J. V. Rodriguez, U. S. Inan, and T. F. Bell, "Heating of the nighttime d region by very low frequency transmitters," *J. Geophys. Res., Space Phys.*, vol. 99, no. A12, pp. 23329–23338, Dec. 1994.

[51] A. M. Wold, R. A. Marshall, D. M. Malaspina, and A. D. Shane, "Prevalence and propagation of lightning-generated whistlers in van Allen probes EFW burst data," *J. Geophys. Res., Space Phys.*, vol. 129, no. 9, p. 2024, Sep. 2024.

[52] A. L. Antunes de Sá and R. A. Marshall, "Lightning distance estimation using LF lightning radio signals via analytical and machine-learned models," *IEEE Trans. Geosci. Remote Sens.*, vol. 58, no. 8, pp. 5892–5907, Aug. 2020.

[53] R. K. Said, U. S. Inan, and K. L. Cummins, "Long-range lightning geolocation using a VLF radio atmospheric waveform bank," *J. Geophys. Res., Atmos.*, vol. 115, no. D23, pp. 1–19, Dec. 2010.

[54] R. K. Said, M. B. Cohen, and U. S. Inan, "Highly intense lightning over the oceans: Estimated peak currents from global GLD360 observations," *J. Geophys. Res., Atmos.*, vol. 118, no. 13, pp. 6905–6915, Jul. 2013.

[55] C. J. Rodger et al., "Detection efficiency of the VLF world-wide lightning location network (WWLLN): Initial case study," *Annales Geophysicae*, vol. 24, no. 12, pp. 3197–3214, Dec. 2006. [Online]. Available: https://angeo.copernicus.org/articles/24/3197/2006/

[56] P. M. Vankawala, R. A. Marshall, D. Vida, and P. Brown, "An observational investigation of very low frequency radio emissions originating from meteors," *Planet. Space Sci.*, vol. 245, Jun. 2024, Art. no. 105892.

[57] R. A. Helliwell, *Whistlers and Related Ionospheric Phenomena*. Stanford, CA, USA: Stanford Univ. Press, 1965.

[58] R. Dowden, J. Brundell, and M. Hayakawa, "Remote sensing by VLF using 'absolute omnipal'. 1. Investigation of short path propagation for possible earthquake precursor detection," in *Proc. Int. Conf. Math. Methods Electromagn. Theory (MMET)*, Jun. 1998, pp. 29–34.

[59] Y. Chen et al., "Development of ground-based ELF/VLF receiver system in Wuhan and its first results," *Adv. Space Res.*, vol. 57, no. 9, pp. 1871–1880, May 2016.

[60] H. Lu, S. Wang, X. Xu, Y. Ji, and X. Liu, "Compact multi-channel longwave wideband direction-finding system and direction-finding analysis for different modulation signals," *Appl. Sci.*, vol. 15, no. 5, p. 2570, Feb. 2025.

[61] M. B. Cohen, U. S. Inan, and E. W. Paschal, "Sensitive broadband ELF/VLF radio reception with the AWESOME instrument," *IEEE Trans. Geosci. Remote Sens.*, vol. 48, no. 1, pp. 3–17, Jan. 2010.

[62] M. B. Cohen et al., "Broadband longwave radio remote sensing instrumentation," *Rev. Scientific Instrum.*, vol. 89, no. 9, pp. 094501-1–094501-18, Sep. 2018.

[63] B. Das and P. K. Haldar, "A brief review of ELF/VLF reception techniques & experiments," in *Advances in Modern and Applied Sciences*. Stanford, CA, USA: Stanford Univ. Press, 2022, p. 146.

[64] *NEO/LEA-M8T: U-Blox M8 Concurrent GNSS Timing Modules*, U-blox AG, Thalwil, Switzerland, 2023.

[65] S. K. Harriman, E. W. Paschal, and U. S. Inan, "Magnetic sensor design for femtotesla low-frequency signals," *IEEE Trans. Geosci. Remote Sens.*, vol. 48, no. 1, pp. 396–402, Jan. 2010.

[66] E. W. Paschal, "The design of broad-band VLF receivers with air-core loop antennas," Dept. Elect. Eng., Stanford University, Stanford, CA, USA, Tech. Rep. 091205, 1980.

[67] E. Paschal, "Pseudo-random waveforms and comb calibration signals," Dept. Elect. Eng., Stanford University, Stanford, CA, USA, Tech. Rep., 2005.

[68] S. W. Golomb, *Shift Register Sequences: Secure and Limited-Access Code Generators, Efficiency Code Generators, Prescribed Property Generators, Mathematical Models*. Singapore: World Scientific, 2017.

[69] R. A. Marshall, T. Wallace, and M. Turbe, "Finite-difference modeling of very-low-frequency propagation in the Earth-ionosphere waveguide," *IEEE Trans. Antennas Propag.*, vol. 65, no. 12, pp. 7185–7197, Dec. 2017.

[70] D. D. Crombie, "On the use of VLF measurements for obtaining information on the lower ionosphere (especially during solar flares)," *Proc. IEEE*, vol. 53, no. 12, pp. 2027–2034, 1965.

[71] M. P. Johnson, U. S. Inan, and D. S. Lauben, "Subionospheric VLF signatures of oblique (nonducted) whistler-induced precipitation," *Geophys. Res. Lett.*, vol. 26, no. 23, pp. 3569–3572, Dec. 1999.

[72] F. Gasdia and R. A. Marshall, "Assimilating VLF transmitter observations with an LETKF for spatial estimates of the *D*-region ionosphere," *IEEE Trans. Geosci. Remote Sens.*, vol. 58, no. 5, pp. 3526–3543, May 2020.

[73] F. Gasdia, "Imaging the d-region ionosphere with subionospheric VLF signals," Ph.D. dissertation, Ann and H.J. Smead Dept. Aerosp. Eng.Sci., University of Colorado at Boulder, Boulder, CO, USA, 2021.

[74] F. Gasdia and R. A. Marshall, "A method for imaging energetic particle precipitation with subionospheric VLF signals," *Earth Space Sci.*, vol. 10, no. 1, p. 2022, Jan. 2023.

[75] H. E. George, C. J. Rodger, M. A. Clilverd, K. Cresswell-Moorcock, J. B. Brundell, and N. R. Thomson, "Developing a nowcasting capability for X-class solar flares using VLF radiowave propagation changes," *Space Weather*, vol. 17, no. 12, pp. 1783–1799, Dec. 2019.

[76] S. Kumar, S. Kumar, and A. Kumar, "Earthquakes associated subionospheric VLF anomalies recorded at two low latitude stations in the South Pacific region," *J. Atmos. Solar-Terrestrial Phys.*, vol. 229, Mar. 2022, Art. no. 105834.

[77] X. Gu et al., "Comparison of VLF signal responses to solar flares along daytime and nighttime propagation paths," *Remote Sens.*, vol. 15, no. 4, p. 1018, Feb. 2023.

[78] J. G. Van Bladel, *Electromagnetic Fields*. Hoboken, NJ, USA: Wiley, 2007.

[79] V. Žigman, M. Dominique, D. Grubor, C. J. Rodger, and M. A. Clilverd, "Lower-ionosphere electron density and effective recombination coefficients from multi-instrument space observations and ground VLF measurements during solar flares," *J. Atmos. Solar-Terrestrial Phys.*, vol. 247, Jun. 2023, Art. no. 106074.

[80] F. Gasdia and R. A. Marshall, "A new longwave mode propagator for the Earth—Ionosphere waveguide," *IEEE Trans. Antennas Propag.*, vol. 69, no. 12, pp. 8675–8688, Dec. 2021.

[81] K. R. Murphy et al., "The global statistical response of the outer radiation belt during geomagnetic storms," *Geophys. Res. Lett.*, vol. 45, no. 9, pp. 3783–3792, May 2018.

[82] J. C. Green, T. G. Onsager, T. P. O'Brien, and D. N. Baker, "Testing loss mechanisms capable of rapidly depleting relativistic electron flux in the Earth's outer radiation belt," *J. Geophys. Res., Space Phys.*, vol. 109, no. A12, pp. 1–12, Dec. 2004.

[83] J. Bortnik and R. M. Thorne, "The dual role of ELF/VLF chorus waves in the acceleration and precipitation of radiation belt electrons," *J. Atmos. Solar-Terrestrial Phys.*, vol. 69, no. 3, pp. 378–386, Mar. 2007.

[84] R. M. Thorne, "Radiation belt dynamics: The importance of wave-particle interactions," *Geophys. Res. Lett.*, vol. 37, no. 22, pp. 1–7, Nov. 2010.

[85] C. A. Loewe and G. W. Prölss, "Classification and mean behavior of magnetic storms," *J. Geophys. Res., Space Phys.*, vol. 102, no. A7, pp. 14209–14213, Jan. 1997.

[86] W. D. González et al., "What is a geomagnetic storm?," *J. Geophys. Res., Space Phys.*, vol. 99, no. 4, pp. 5771–5792, 1994.